



IV

Publication IV

F. Boxberg, R. Tereshonkov and J. Tulkki, *Polarization of gain and symmetry breaking by interband coupling in quantum well lasers*, *Journal of Applied Physics* **100**, 063108 (2006).

© 2006 American Institute of Physics

Reprinted with permission.

Polarization of gain and symmetry breaking by interband coupling in quantum well lasers

Fredrik Boxberg,^{a)} Roman Tereshonkov, and Jukka Tulkki

Laboratory of Computational Engineering, Helsinki University of Technology, FIN-02015 HUT, Finland

(Received 20 June 2006; accepted 27 June 2006; published online 26 September 2006)

We have studied the influence of conduction band–valence band coupling on the polarization of gain in quantum well (QW) lasers. As a reference we used the eight-band $\mathbf{k}\cdot\mathbf{p}$ description of the gain polarization. Our eight-band $\mathbf{k}\cdot\mathbf{p}$ model accounts for the crystal orientation, lack of inversion symmetry, strain induced deformation potentials, and piezoelectricity. We have studied both strained and unstrained (001) and (111) QWs. The results are compared with the transition dipole model of the gain polarization [M. Asada *et al.*, IEEE J. Quantum Electron. **20**, 745 (1984)], which is based on a phenomenological generalization of Kane's [J. Phys. Chem. Solids **1**, 249 (1957)] linear $\mathbf{k}\cdot\mathbf{p}$ model of bulk crystals. We found a quantitative difference between our multiband model and the transition dipole model of Asada *et al.* The difference is addressed to lack of orthogonality between the transition dipole and the electron wave vectors. The orthogonality is broken outside the Γ point by both the QW heterostructure geometry and the interband coupling. Results obtained by the complete eight-band model are also compared with restricted multiband models excluding the conduction band. © 2006 American Institute of Physics.

[DOI: 10.1063/1.2353276]

I. INTRODUCTION

The polarization of gain is an important physical characteristic of semiconductor lasers. In spite of its fundamental significance, the polarization of gain in quantum well (QW) lasers has so far not been analyzed within a multiband model that would include all the strongly coupled valence and conduction bands of III-V compound semiconductors. Accordingly the gain polarization in semiconductor lasers is as a rule analyzed within the lowest order, parabolic-band model of Asada and co-workers^{1–4} or with restricted four-valence-band^{5,6} and six-valence-band $\mathbf{k}\cdot\mathbf{p}$ models,^{7,8} which do not include the important symmetry breaking effect of the conduction band. Gershoni *et al.*⁹ have also used the eight-band $\mathbf{k}\cdot\mathbf{p}$ model to calculate the gain in QWs. However, they did not include a discussion of the polarization of gain in their work. Hader *et al.* have also made extensive work on the modeling of the transverse electric mode (TE) gain in semiconductor QW lasers (see, e.g., Refs. 10–12 and references therein). Their approach is based on semiconductor Bloch equations together with the eight-band $\mathbf{k}\cdot\mathbf{p}$ theory. It includes interband Coulomb correlations and band-gap renormalization in second order Born approximation, but Hader *et al.* did not discuss the polarization of gain in their work. This has prompted us to make a detailed analysis of the gain polarization by the eight-band $\mathbf{k}\cdot\mathbf{p}$ model, which is known to give an accurate description of the electronic states close to the band edges in III-V semiconductors and their heterostructures. We also compare the results of this reference model with approximate single and multiband effective-mass gain models, in order to explore the accuracy of these widely used gain polarization models.

The parabolic band Asada, Kameyama, and Suematsu (AKS) model¹ was based on Kane's linearized eight-band $\mathbf{k}\cdot\mathbf{p}$ model,¹³ for bulk semiconductors. In this model the polarization of gain is governed by the breaking of the heavy-hole (HH) band symmetry, by the coupling of the conduction and valence bands. It explains the polarization of gain using a geometrical relationship between the transition dipole and the electron wave vector. This simple and transparent physical interpretation of the gain polarization has made it the “standard model” in the modeling of semiconductor lasers. The AKS model has also been reported to be in good agreement with experiments.¹⁴ This is surprising, since its possible validity is restricted to the near-band-edge regime of bulk semiconductors and its use for QW lasers is based on phenomenological arguments only.

In this work we show that the polarization of gain in QW lasers can be calculated accurately with a $\mathbf{k}\cdot\mathbf{p}$ model only by including eight bands or more. Our eight-band $\mathbf{k}\cdot\mathbf{p}$ model includes strain and piezoelectric effects and allows analysis of arbitrarily oriented QWs. We have studied four different QW geometries, QW1: a lattice-matched Ga_{0.47}In_{0.53}As/Al_{0.48}In_{0.52}As (001) QW, QW2: a strained Ga_{0.47}In_{0.53}As/Al_{0.33}In_{0.67}As (001) QW, QW3: a lattice-matched Ga_{0.47}In_{0.53}As/Al_{0.48}In_{0.52}As (111) QW and, QW4: a strained Ga_{0.47}In_{0.53}As/Al_{0.33}In_{0.67}As (111) QW. The width of the QWs was 10 nm. In QW2 and QW4, the QW was under 1% tensile strain while the barrier was strain-free. These material compositions were selected for the sake of the availability of good and consistent eight-band $\mathbf{k}\cdot\mathbf{p}$ material parameters as well as high quality reference calculations¹⁵ of electronic structure in the pertinent QWs. The $\mathbf{k}\cdot\mathbf{p}$ parameters, used in the calculations, are based on pseudopotential reference calculations and enable eight-band $\mathbf{k}\cdot\mathbf{p}$ calculations without any numerical inconsistencies or artificial, rapidly oscillating

^{a)}Electronic mail: fredrik.boxberg@tkk.fi

eigenstates (see, e.g., Ref. 16). The dimensions and materials of the selected QWs were not optimized for technological laser applications. However, our results are well representative for gain polarization in QW lasers made of III-V compound semiconductors in general.

The paper is organized as follows: In Sec. II, we review the AKS model, including the electronic structure and the gain of bulk material and QWs. In Sec. III we describe our eight-band $\mathbf{k}\cdot\mathbf{p}$ model for the material gain and its polarization. Then in Sec. IV we compare the polarization of gain in different models, discussing both bulk semiconductors and QWs. Finally in Sec. V we draw conclusions and discuss the validity of different models.

II. THE AKS MODEL

The AKS model,¹ for the polarization of gain in semiconductor lasers, is based on Kane's linearized eight-band $\mathbf{k}\cdot\mathbf{p}$ Hamiltonian¹³ for bulk semiconductors. In Refs. 1, 17, and 18 a simple geometrical relation was derived between (1) the polarization of stimulated emission, (2) the electron wave vector \mathbf{k} , and (3) the electric dipole moment \mathbf{R}_{cv} of the electron transition (transition dipole). It was shown that for a conduction-HH band transition in bulk semiconductors, \mathbf{R}_{cv} has to be perpendicular to the initial (and final) electron wave vector \mathbf{k} . The geometrical relation was generalized for QWs. This, however, required a phenomenological redefinition of the electron wave vector. Its vector component k_z , orthogonal to the QW, was replaced by $k_z \rightarrow \sqrt{2m_C^*E_{Cn}}/\hbar = \sqrt{2m_{HH}^*E_{HHn}}/\hbar$, where m_C^* (m_{HH}^*) is the effective mass in the conduction (HH) band and E_{Cn} (E_{HHn}) is the confinement energy of the n th conduction (HH) band. The defined k_z is analogous to the wave number of a sinusoidal standing wave between infinite potential barriers.

A. AKS model for bulk semiconductors

In Kane's linear eight-band $\mathbf{k}\cdot\mathbf{p}$ model¹³ the off-diagonal Hamiltonian terms, proportional to k^2 , were omitted (see Appendix for a brief introduction to the $\mathbf{k}\cdot\mathbf{p}$ model). In order to diagonalize the linearized Hamiltonian for arbitrary \mathbf{k} , Kane applied a coordinate transformation bringing z axis parallel to \mathbf{k} . This transformation diagonalizes the HH part of the eight-band Hamiltonian. The conduction band remains weakly coupled to the light-hole (LH) band. However, these remaining coupling terms are proportional to \mathbf{k} and small in the vicinity of the Γ point.

The coordinate transformation depends on the direction of \mathbf{k} and the new eigenstates are linear combinations of the basis functions given in the crystal coordinates. The transition dipole between the rotated conduction $|\Psi_C\rangle'$ and HH $|\Psi_{HH}\rangle'$ states is given by

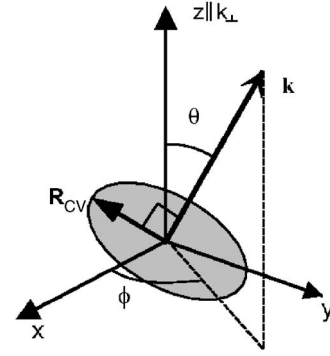


FIG. 1. The assumed geometric relation between the electron wave vector \mathbf{k} and the transition dipole \mathbf{R}_{cv} . For transitions between the conduction band and the HH band, the transition dipole becomes orthogonal to the wave vector.

$$\mathbf{R}_{cv} = \langle \Psi_C |' e\mathbf{r} | \Psi_{HH} \rangle' = \begin{cases} R(\cos \theta \cos \phi - i \sin \phi), & \hat{\mathbf{u}}_x \\ R(\cos \theta \sin \phi + i \cos \phi), & \hat{\mathbf{u}}_y \\ -R \sin \theta, & \hat{\mathbf{u}}_z \end{cases} \quad (1)$$

where θ and ϕ are the spherical polar coordinates of \mathbf{k} and $\hat{\mathbf{u}}_i$ are the unit vectors of the main crystallographic axes. The length of \mathbf{R}_{cv} is given by

$$R = \frac{e\hbar}{\sqrt{2}m_0E_g} |\langle S | p_x | X \rangle|, \quad (2)$$

where E_g is the band gap energy. The momentum matrix element $\langle S | p_x | X \rangle$ is related to the $\mathbf{k}\cdot\mathbf{p}$ parameter E_p through $|\langle S | p_x | X \rangle| = \sqrt{m_0}E_p/2$. From Eq. (1) we see that the transition dipole is perpendicular to the electron wave vector, i.e., $\mathbf{k}\cdot\mathbf{R}_{cv}=0$, where the wave vector can be written as $\mathbf{k} = k \sin \theta \cos \phi \hat{\mathbf{u}}_x + k \sin \theta \sin \phi \hat{\mathbf{u}}_y + k \cos \theta \hat{\mathbf{u}}_z$ in the Cartesian coordinates. Figure 1 shows schematically the geometrical relations between \mathbf{k} and \mathbf{R}_{cv} as well as the definitions of the spherical coordinates ϕ and θ .

B. AKS model for quantum wells

In a QW perpendicular to the z axis, the electron wave vector $\mathbf{k}=\mathbf{k}_{\parallel}$ restricted to the plane of the QW because the expectation value of its z component is zero,

$$\langle k_z \rangle = \left\langle -i\hbar \frac{\partial}{\partial z} \right\rangle = 0. \quad (3)$$

However, it contributes still to the interband coupling of the envelope Hamiltonian via terms proportional to $\partial/\partial z$ and $\partial^2/\partial z^2$. These terms are not necessarily small even for small \mathbf{k}_{\parallel} and cannot be eliminated by a coordinate transformation. The eight-band $\mathbf{k}\cdot\mathbf{p}$ envelope Hamiltonian of a QW can therefore not be diagonalized in the same way as the bulk Hamiltonian. Asada *et al.* assumed that one can account for the QW confinement in the following way. Instead of using k_z , given by Eq. (3), in the coordinate transformation they defined an *effective* k_z vector component as

$$\tilde{k}_z \equiv \sqrt{\frac{2m_C^* E_{Cn}}{\hbar^2}} = \sqrt{\frac{2m_{\text{HH}}^* E_{\text{HH}n}}{\hbar^2}}, \quad (4)$$

where m_C^* (m_{HH}^*) is the effective mass in the conduction (HH) band and E_{Cn} ($E_{\text{HH}n}$) is the confinement energy of the n th conduction (HH) band. This was based on the analogy to the wave number of a standing wave in a square well potential. The QW Hamiltonian was diagonalized by a coordinate transformation that makes use of the phenomenological wave vector $\mathbf{k}=[k_x, k_y, \tilde{k}_z]$ and brings $\hat{\mathbf{u}}_z \parallel \mathbf{k}$. Under this assumption the decoupled conduction and HH eigenstates are given by

$$\begin{aligned} \Psi_{Cn}(\mathbf{r}, \mathbf{k}) &= \sum_v \phi_v^{Cn}(z, \mathbf{k}) |u_v\rangle \\ &\approx \phi_c^{Cn}(z) \sum_v C_v^{Cn}(\mathbf{k}) |u_v\rangle \\ &= \phi_c^{Cn}(z) |u_c(\mathbf{k})\rangle', \end{aligned} \quad (5a)$$

$$\Psi_{\text{HH}m}(\mathbf{r}, \mathbf{k}) \approx \phi_{\text{hh}}^{\text{HH}m}(z) |u_{\text{hh}}(\mathbf{k})\rangle', \quad (5b)$$

where Ψ is the total wave function, ϕ are the envelope wave functions, $|u_l(\mathbf{k})\rangle'$ are the bulk Γ -point Bloch functions, and the primes indicate that the states are expressed using the rotated coordinate system (see Ref. 13 for more details on the coordinate transformation). This implies that only the Bloch functions are rotated according to \mathbf{k} , whereas the envelope wave functions of the conduction and HH bands are independent of the rotation. In the notation ϕ_l^m for the envelope wave functions, the subindices refer to the Γ -point Bloch function component and the upper indices refer to the subbands composed from the Γ -point Bloch functions. The envelope wave functions were solved using a parabolic one-band effective-mass Hamiltonian.

C. AKS model for the polarization of gain in quantum well lasers

The material gain of a QW is based on the transition amplitudes between electron and hole states

$$\begin{aligned} \mathbf{R}_{Cn, \text{HH}m} &= \langle \Psi_{Cn}(\mathbf{r}, \mathbf{k}_{Cn}) | e \mathbf{r} | \Psi_{\text{HH}m}(\mathbf{r}, \mathbf{k}_{\text{HH}m}) \rangle \delta_{\mathbf{k}_{Cn}, \mathbf{k}_{\text{HH}m}} \\ &\approx \langle \phi_c^{Cn}(z) | \phi_{\text{hh}}^{\text{HH}m}(z) \rangle \langle u_c(\mathbf{r}, \mathbf{k}) | e \mathbf{r} | u_{\text{hh}}(\mathbf{r}, \mathbf{k}) \rangle'. \end{aligned} \quad (6)$$

In the parabolic band model only diagonal transitions are allowed, because of the orthogonality between the electron and hole envelope wave functions, i.e.,

$$\langle \phi_c^{Cn}(z) | \phi_{\text{hh}}^{\text{HH}m}(z) \rangle \approx \delta_{nm}. \quad (7)$$

It follows now that the transition dipole is given by Eq. (1), except that the spherical coordinates of the electron wave vector are replaced by

$$\cos \theta = \sqrt{\frac{E_{Cn}}{\hbar^2 \mathbf{k}_{\parallel}^2 / 2m_C^* + E_{Cn}}}, \quad (8a)$$

$$\tan \phi = \frac{k_y}{k_x}. \quad (8b)$$

The material gain is obtained by summing the squares of all diagonal transition amplitudes multiplied by the pertinent

Fermi functions. The integration of the squared transition amplitudes over \mathbf{k}_{\parallel} can be changed to an integration over the transition energy $E_{\text{ch}} = E_{Cn} - E_{\text{HH}n}$. This is done by averaging the squares of the amplitudes over ϕ and introducing the density of states (DOS) of parabolic bands. The averaged transition dipoles are given by

$$\begin{aligned} \langle \mathbf{R}^2 \rangle_n &= \frac{1}{2\pi} \int_0^{2\pi} |\boldsymbol{\varepsilon} \cdot \mathbf{R}_{Cn, \text{HH}n}|^2 d\phi \\ &= \begin{cases} R^2 \frac{1}{2} (1 + \cos^2 \theta) & \text{for } \boldsymbol{\varepsilon}_{\parallel} \\ R^2 \sin^2 \theta & \text{for } \boldsymbol{\varepsilon}_{\perp}, \end{cases} \end{aligned} \quad (9)$$

where $\boldsymbol{\varepsilon}$ is the unit polarization vector of the photon field and θ is given by Eq. (8a). The total material gain is now given by

$$\begin{aligned} G(E) &= \frac{\omega \sqrt{\mu} \varepsilon m_C^* m_{\text{HH}}^*}{\pi \hbar^2 L (m_C^* + m_{\text{HH}}^*)} \\ &\times \sum_n \int \frac{\langle \mathbf{R}^2 \rangle_n [f_e(E_{Cn}) - f_h(E_{\text{HH}n})] \Gamma}{(E_{\text{ch}} - E)^2 + \Gamma^2} dE_{\text{ch}}, \end{aligned} \quad (10)$$

where μ is the permeability, ε is the permittivity, m_{hh}^* is the DOS mass of the HH band, L is the width of the QW, f_e (f_h) is the Fermi function of electrons (holes), and Γ is the homogeneous linewidth broadening. The material gain depends on the polarization through the polarization vector $\boldsymbol{\varepsilon}$ in Eq. (9) although this is not shown explicitly in Eq. (10). The LH bands were omitted from the AKS gain model, since the density of states is a lot smaller for the LH band than for the HH band.

D. The effect of the light-hole band in the AKS model

The phenomenological model of Asada *et al.* was generalized by Yamanishi and Suemune to include also the conduction (C) to LH band transitions in the material gain.¹⁷ The C-LH transition dipoles were obtained by replacing the rotated HH eigenstates of Eq. (1) by rotated LH states. The small residual coupling of the Hamiltonian between the conduction and LH band was neglected. Following Ref. 13, we obtain the following transition amplitudes (averaged over ϕ) for the C-LH transitions:

$$\frac{1}{2\pi} \int_0^{2\pi} |\boldsymbol{\varepsilon} \cdot \mathbf{R}_{Cn, \text{LH}m}|^2 d\phi = \begin{cases} R^2 \frac{1}{6} (5 - 3 \cos^2 \theta) & \text{for } \boldsymbol{\varepsilon}_{\parallel} \\ R^2 \frac{1}{3} (1 + 3 \cos^2 \theta) & \text{for } \boldsymbol{\varepsilon}_{\perp}. \end{cases} \quad (11)$$

In Ref. 17 the transition dipoles were given with respect to the corresponding averaged transition dipoles for bulk; $M = 2R^2/3$. Yamanishi and Suemune¹⁷ did not present a complete gain model or numerical results for the material. They only “estimated” the material gain of the model, according to experimental results.

III. POLARIZATION OF GAIN WITH THE EIGHT-BAND $\mathbf{k} \cdot \mathbf{p}$ MODEL

In this work we used the eight-band $\mathbf{k} \cdot \mathbf{p}$ envelope Hamiltonian of Ref. 19, generalized to account for the lack of inversion symmetry of zinc blende crystals.¹³ We ac-

TABLE I. Material parameters used (Refs. 22 and 23).

	Ga _{1-x} In _x As x=0.53	Al _{1-y} In _y As	
		y=0.52	y=0.67
E_g (eV)	1.52	0.79	1.12
Δ (eV)	0.36	0.33	0.35
E_p (eV)	16.54	16.46	16.17
m_e^* (m_0)	0.051	0.090	0.070
γ_1^I	8.39	5.02	6.20
γ_2^I	3.24	1.55	2.15
γ_3^I	3.79	2.11	2.70
B (10^{-40} J m ²)	2.74	2.74	2.99
a_0 (Å)	5.87	5.87	5.93
c_{11} (10^{11} dyn cm ⁻²)	9.97	10.00	9.48
c_{12} (10^{11} dyn cm ⁻²)	4.90	4.91	4.79
c_{44} (10^{11} dyn cm ⁻²)	4.88	4.90	4.61
a_c (eV)	-6.94	-6.97	-6.60
a_v (eV)	0.00	0.00	0.00
b_v (eV)	-1.70	-1.70	-1.70
d_v (eV)	5.20	5.20	5.20
ϵ_r (ϵ_0)	12.68	12.68	12.68
e_{14} (C m ⁻²)	-0.10	-0.10	-0.08
m_e^{DOS} (m_0)		0.090	0.090
m_h^{DOS} (m_0)		0.521	0.521

counted for the strain up to zeroth order in \mathbf{k} . Our approach is thereby equivalent to that of Mailhot and Smith.²⁰ We solved the eight-band $\mathbf{k}\cdot\mathbf{p}$ envelope Hamiltonian using the finite difference technique (see, e.g., Ref. 21) with periodic boundary conditions. The numerical methods and the used Hamiltonian are described in the Appendix. All material parameters were taken from Refs. 22 and 23 and are listed in Table I.

The strain of the QWs was calculated using the continuum elasticity (CE) theory.^{15,24} We assumed that the thickness of the QW is a lot smaller than the thickness of the barrier (=substrate). As a result, only the QW is strained and the infinitely large barrier is stress-free. Our previous comparison of the CE with the atomistic valence force-field method showed that the CE is very accurate for these QW structures.²⁴

A. Band structure of quantum wells

The band structure was computed, for the four different QW structures; QW1, QW2, QW3, and QW4 (defined in Sec. I). Regarding the electronic structure our results agree well with previous works.¹⁵

1. (001) quantum wells

Figure 2(a) shows the band edges of the (001) QWs, excluding all strain effects. Figures 3(a) and 3(c) show the probability densities of the ground states in QW1 and QW2, respectively. The carrier densities are wider in the strained QW and the wave functions penetrate the barriers more than in the lattice-matched structure, due to smaller band edge offsets between Ga_{0.47}In_{0.53}As and Al_{0.33}In_{0.67}As (see Fig. 2). Figures 4(a) and 4(b) show the energy bands of QW1 and QW2, respectively.

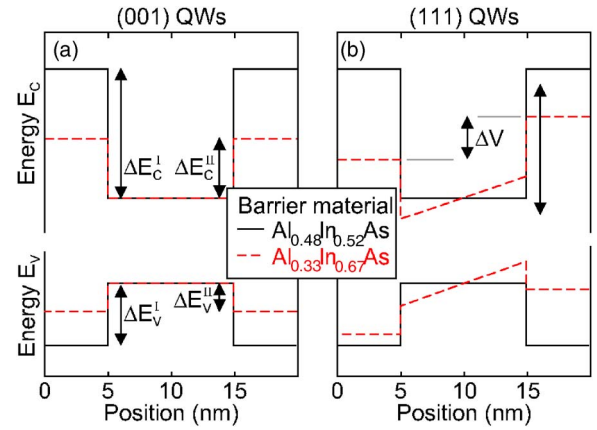


FIG. 2. (Color online) Conduction and valence band edges of (a) the (001) and (b) the (111) QWs. For the lattice-matched QWs (solid lines), the band-edge offsets were $\Delta E_c^I=500$ meV and $\Delta E_v^I=-230$ meV. The offsets for the strained QWs (dashed lines) were $\Delta E_c^I=226$ meV and $\Delta E_v^I=-104$ meV.

2. (111) quantum wells

Figure 2(b) shows the band edges of the (111) QWs. The band edges of QW3 (solid lines) are the same as those of QW1. However, the strained QW4 (dashed lines) acquires an additional piezoelectric field in comparison with the band edges of QW2. The strength of the electric field was $\Delta V=16.5$ meV/nm. Figures 3(b) and 3(d) show the carrier densities in QW3 and QW4, respectively. Figure 5 shows the energy bands of QW3 and QW4. The band gap of the active material is reduced by the strain and by the piezoelectric field. However, the field also lowers the barriers (see Fig. 2) decreasing the effective QW confinement energy in the strained and (111) orientated QW4.

B. Density of states

The material gain is primarily shaped by the DOS and the availability of states that can take part in the recombination process. Even if the material gain is a combined result of the DOS and the transition amplitudes, the fine-tuning of semiconductor QW lasers is in practice realized only by modifying the shape of the DOS and its energy band gap.

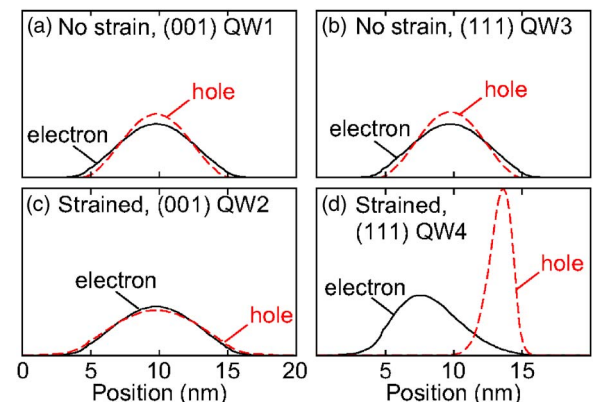


FIG. 3. (Color online) Probability densities of electrons and holes in (a) a lattice-matched (001) QW, (b) a strained (001) QW, (c) a lattice-matched (111) QW, and (d) a strained (111) QW. The solid and dashed lines correspond to electron and hole densities, respectively.

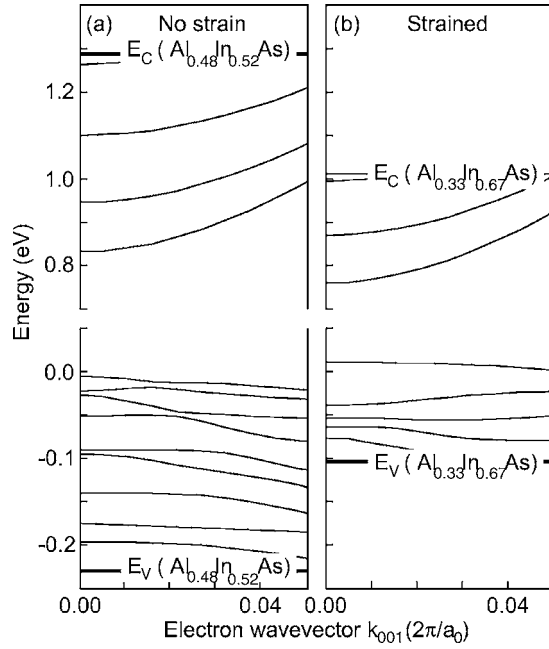


FIG. 4. Energy bands of (a) a lattice-matched $\text{Ga}_{0.47}\text{In}_{0.53}\text{As}/\text{Al}_{0.48}\text{In}_{0.52}\text{As}$ (001) QW and (b) a strained $\text{Ga}_{0.47}\text{In}_{0.53}\text{As}/\text{Al}_{0.33}\text{In}_{0.67}\text{As}$ (001) QW. The thick horizontal lines show the position of the barrier band edge.

The density of states (DOS) per area of the QW was calculated by integrating over \mathbf{k}_{\parallel} and summing over the pertinent subbands²⁵

$$g_C^{\text{QW}}(E) = \sum_n \int_{E_{Cn}(\mathbf{k}_{\parallel}) < E_{C,B}} \frac{d\mathbf{k}_{\parallel}^2}{(2\pi)^2} \delta[E_{Cn}(\mathbf{k}_{\parallel}) - E], \quad (12)$$

where the sum over n contains also the summation over spin. The total DOS of the system was obtained by adding the

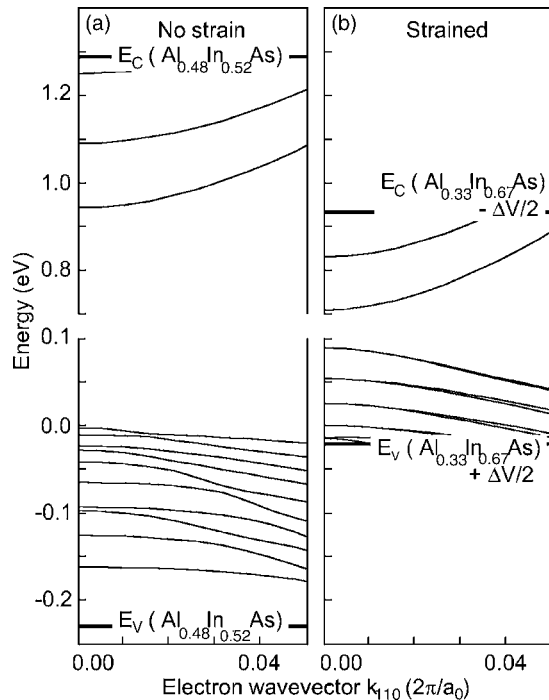


FIG. 5. Energy bands of (a) a lattice-matched $\text{Ga}_{0.47}\text{In}_{0.53}\text{As}/\text{Al}_{0.48}\text{In}_{0.52}\text{As}$ (111) QW and (b) a strained $\text{Ga}_{0.47}\text{In}_{0.53}\text{As}/\text{Al}_{0.33}\text{In}_{0.67}\text{As}$ (111) QW. The thick horizontal lines show the position of the lower barrier band edge.

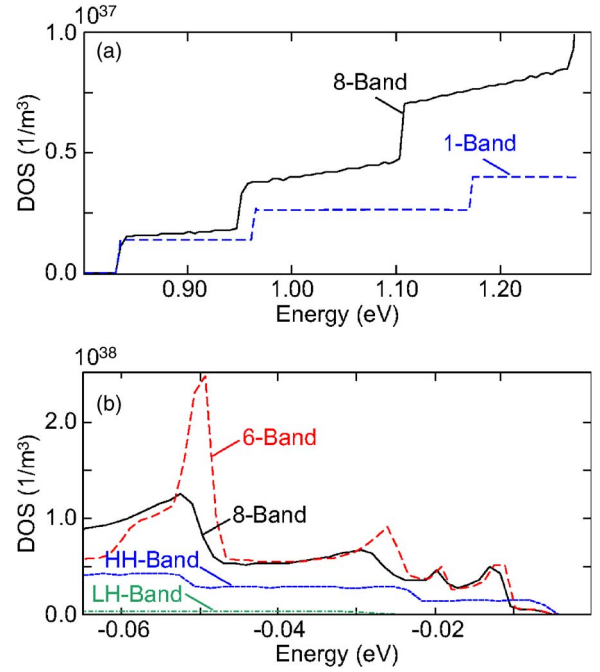


FIG. 6. (Color online) Density of states of (a) electrons and (b) holes in a lattice-matched (001) QW in different models.

continuum of three-dimensional barrier states to the QW DOS

$$g_C(E) = \frac{\sqrt{2}m_{e,B}^{3/2}W_B}{\pi^2\hbar^3} \sqrt{E - E_{C,B}} + \sum_n \int_{E_{Cn}(\mathbf{k}_{\parallel}) < E_{C,B}} \frac{d\mathbf{k}_{\parallel}^2}{(2\pi)^2} \delta[E_{Cn}(\mathbf{k}_{\parallel}) - E], \quad (13)$$

where $m_{e,B}$ is the effective density of states mass of electrons in the barrier, W_B is the width of the barrier, and $E_{C,B}$ is the conduction band edge of the barrier material. A similar expression is obtained for the DOS of the valence bands

$$g_V(E) = \frac{\sqrt{2}m_{h,B}^{3/2}W_B}{\pi^2\hbar^3} \sqrt{E_{V,B} - E} + \sum_n \int_{E_{Vn}(\mathbf{k}_{\parallel}) > E_{V,B}} \frac{d\mathbf{k}_{\parallel}^2}{(2\pi)^2} \delta[E_{Vn}(\mathbf{k}_{\parallel}) - E], \quad (14)$$

where $m_{h,B}$ is the effective density of states mass of holes in the barrier, and $E_{V,B}$ is the valence band edge of the barrier material. The quasi-Fermi energy of electrons (holes) was calculated iteratively by fixing the charge density N_e (N_h), and integrating over the DOS multiplied by the Fermi function.

The numerically calculated DOS of QW1 is shown in Fig. 6. The DOS was calculated from the energy bands obtained with the eight-band (“8-band”), six-band (“6-band”), and AKS (“HH-band”) models. The DOS of the AKS model is smaller than those of the six- and eight-band models mainly because the valence band mixing was omitted from the AKS model. The band structures of the six- and eight-band models are very similar close to the band edges; however, at higher energies and higher \mathbf{k} values the differences increase. As a result the DOSs of the valence bands are very

similar down to $E = -0.05$ eV. At this point the six-band model shows a large peak and exceeds the eight-band model by a factor of 2. The large peak of the six-band DOS is a result of very flat valence bands in this energy range.

In the conduction band DOS, the $\mathbf{k} \cdot \mathbf{p}$ coupling of the conduction and valence bands is seen as slanted staircases, because the conduction bands obtained from the eight-band model are slightly flatter than those of the parabolic band model. The DOS is not sensitive to the symmetry change caused by the coupling of conduction and valence bands, due to the averaging over the direction of the wave vector.

C. The polarization of material gain

The material gain was calculated by integrating the transition rates over \mathbf{k}_{\parallel} for all interband transitions. All transition rates were weighted by the corresponding population factor $\{f_e[E_{Cn}(\mathbf{k}_{\parallel})] - f_h[E_{Vm}(\mathbf{k}_{\parallel})]\}$. The total material gain, as a function of energy E , is then given by

$$G(E) = \frac{e^2 \hbar}{2\pi^2 m_0^2 L E} \sqrt{\frac{\mu}{\varepsilon}} \sum_{n,m} \int d\mathbf{k}_{\parallel} |W_{Cn,Vm}|^2 \times \frac{\{f_e[E_{Cn}(\mathbf{k}_{\parallel})] - f_h[E_{Vm}(\mathbf{k}_{\parallel})]\} \Gamma}{[E_{Cn}(\mathbf{k}_{\parallel}) - E_{Vm}(\mathbf{k}_{\parallel}) - E]^2 + \Gamma^2}, \quad (15)$$

where Γ is the linewidth broadening. Two different forms for the transition amplitude $W_{Cn,Vm}$ have been used in the literature (see, e.g., Refs. 9, 19, and 26):

$$W_{Cn,Vm} = \begin{cases} \boldsymbol{\varepsilon} \cdot \left\langle \phi_{Cn} \left| \frac{m_0}{\hbar} (\nabla_k \hat{H}) \right| \phi_{Vm} \right\rangle \\ \boldsymbol{\varepsilon} \cdot \langle \Psi_{Cn} | -i\hbar \nabla | \Psi_{Vm} \rangle, \end{cases} \quad (16)$$

where \hat{H} is the eight-band $\mathbf{k} \cdot \mathbf{p}$ envelope Hamiltonian, Ψ_i are the complete eight-band $\mathbf{k} \cdot \mathbf{p}$ wave functions, and ϕ_i are the envelope wave functions. However, the differences between the gain profiles obtained by these two transition rates were very small.

In the following, we use $\boldsymbol{\varepsilon}_{\perp}$ (equals the transverse magnetic mode: TM) polarization for an electric field perpendicular to the QW plane and $\boldsymbol{\varepsilon}_{\parallel}$ (TE) for an electric field in the QW plane. Figures 7(a) and 7(b) show the material gain of an (001) QW at $T = 300$ K for the $\boldsymbol{\varepsilon}_{\perp}$ and $\boldsymbol{\varepsilon}_{\parallel}$ polarizations, respectively. The solid lines correspond to zero linewidth and the dashed lines to a homogeneous linewidth of $\Gamma = 6.6$ meV. The gain was computed for three different carrier concentrations $N_e = N_h = 3 \times 10^{18}, 5 \times 10^{18}, 7 \times 10^{18} \text{ cm}^{-3}$. The gain of the $\boldsymbol{\varepsilon}_{\parallel}$ polarized light is dominated by the $C1 \rightarrow \text{HH1}$ transition (HHn refers to the n th valence band with HH character), while that of the $\boldsymbol{\varepsilon}_{\perp}$ polarized light is dominated by the $C1 \rightarrow \text{LH1}$ transition (LHn refers to the n th valence band with LH character and in general $\text{LH1} \neq \text{V1}$).

The gain increases with increasing carrier density for all QWs. In the lattice-matched QWs the magnitude of the peak gain is larger for the $\boldsymbol{\varepsilon}_{\parallel}$ (TE) polarization than for the $\boldsymbol{\varepsilon}_{\perp}$ (TM). The sharp peak at $\lambda \approx 1.275 \mu\text{m}$ for $N = 7 \times 10^{18} \text{ cm}^{-3}$ in the $\boldsymbol{\varepsilon}_{\parallel}$ polarized gain is due to the diagonal transition $C2 \rightarrow \text{V2}$. This transition was not seen in the gain of $\boldsymbol{\varepsilon}_{\perp}$ polarized light and the influence of this transition on the gain profile increases with increasing carrier densities.

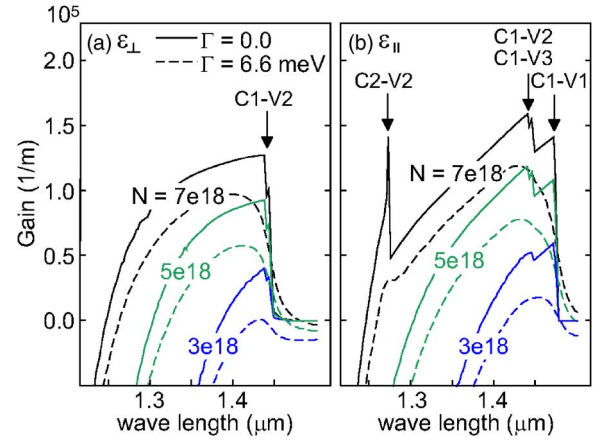


FIG. 7. (Color online) Material gain, using the eight-band $\mathbf{k} \cdot \mathbf{p}$ model, at $T = 300$ K for polarizations (a) $\boldsymbol{\varepsilon}_{\perp}$ (TM) and (b) $\boldsymbol{\varepsilon}_{\parallel}$ (TE) in a lattice-matched and (001) oriented QW for different charge carrier densities $N = N_e = N_h = 3 \times 10^{18}, 5 \times 10^{18}, 7 \times 10^{18} \text{ cm}^{-3}$. The solid lines correspond to zero linewidth and the dashed to a linewidth of $\Gamma = 6.6$ meV.

Figures 8(a) and 8(b) show the material gain in different QWs for $\boldsymbol{\varepsilon}_{\perp}$ and $\boldsymbol{\varepsilon}_{\parallel}$ polarizations, respectively. The solid lines correspond to (001) oriented QWs and the dashed lines to (111) oriented QWs. The gain profiles of strained and lattice-matched (“no strain”) are shown by labels. For (001) QWs the tensile strain (QW2) decreases the gain of $\boldsymbol{\varepsilon}_{\parallel}$ polarized light while that of $\boldsymbol{\varepsilon}_{\perp}$ polarized light is enhanced, because the tensile strain shifts the LH states upwards with respect to the HH states, enhancing the $\boldsymbol{\varepsilon}_{\perp}$ gain, dominated by the $C1 \rightarrow \text{LH1}$ transition. Moreover, in the QW2 structure, the wave function overlap between the electron and hole ground states is larger than in QW1, increasing the gain further. The material gain of QW3 is very similar to that of QW1. However, the strained QW4 differs remarkably from the other structures, due to the piezoelectric field. The field ruins the $\boldsymbol{\varepsilon}_{\perp}$ polarized material gain completely. The $\boldsymbol{\varepsilon}_{\parallel}$ gain is still visible in the 10 nm wide QW4, but the gain profile is very broad. We note, however, that a thorough description of the material gain of strained and piezoelectric (111) QWs would require self-consistent Poisson-Hamiltonian calculations of the charge distribution. This is, however, out of the scope of the current work.

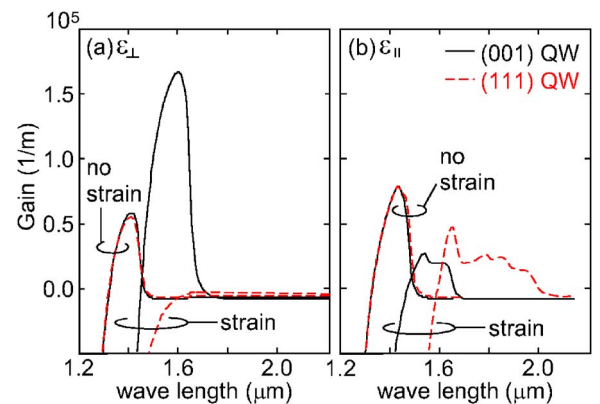


FIG. 8. (Color online) Material gain, using the eight-band $\mathbf{k} \cdot \mathbf{p}$ model, in the QW1–QW4 structures (as explained in the text) for (a) $\boldsymbol{\varepsilon}_{\perp}$ and (b) $\boldsymbol{\varepsilon}_{\parallel}$ polarizations. The solid and dashed lines correspond to (001) and (111) oriented QWs, respectively. The gain of the tensile QW becomes redshifted due to the increased band gap.

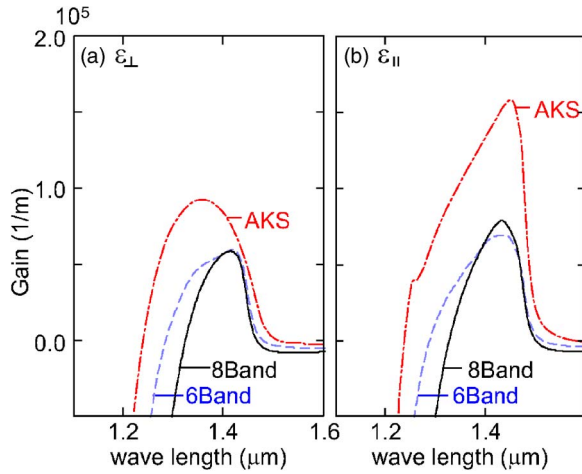


FIG. 9. (Color online) Material gain, using different models for (a) ϵ_{\perp} and (b) ϵ_{\parallel} polarizations in a lattice-matched and (001) oriented QW. The highest gain was obtained using the AKS gain model (dash-dotted lines) whereas the six-band (dashed) and eight-band (solid) models yielded very similar gain profiles. The difference in the gain, between the AKS model and the AKS model including both HH and LH (not coupled) valence band gain of the AKS model was of the same order as the line thickness. All results correspond to a linewidth of $\Gamma=6.6$ meV and a charge carrier density of $N=5 \times 10^{18}$ cm $^{-3}$.

IV. COMPARISON OF THE POLARIZATION OF GAIN IN AKS AND MULTIBAND MODELS

A. Bulk semiconductor

We first compared the AKS model for bulk semiconductors with the full eight-band $\mathbf{k} \cdot \mathbf{p}$ model and found it very accurate for $\mathbf{k} < 0.02 \times k_{Bz}$ (i.e., 2% of the edge of the first Brillouin zone), which is certainly the upper limit of any linear model. The mixing coefficients of the HH band are not affected by the linearization in this regime, whereas the mixing coefficients of the other bands are changed by a few percent. The LH band is most sensitive to the linearization. The linearized model yields about 7 meV greater conduction band energy and 5 meV greater HH energy (i.e., 2 meV larger energy separation between the conduction and HH bands) at $\mathbf{k}=0.02 \times k_{Bz}$ of bulk GaAs.

We estimated also the error of the transition amplitude for bulk GaAs. A comparison of the AKS model with the complete eight-band $\mathbf{k} \cdot \mathbf{p}$ model shows that the error in the length of the transition dipole [Eq. (2)] is less than 1% for $k \leq 0.02 \times k_{Bz}$. The linearized model yields in general larger transition amplitudes than the full eight-band $\mathbf{k} \cdot \mathbf{p}$ model, because the additional band coupling reduces the transition dipole. We conclude that Kane's linear approximation, as used in the AKS model, is certainly reasonable for small and moderate carrier densities in *bulk* semiconductors.

B. Quantum wells

Figure 9 shows the material gain obtained with different models for the QW1 structure. Figures 9(a) and 9(b) correspond to the gain for ϵ_{\parallel} and ϵ_{\perp} polarized light correspondingly. All curves include a homogeneous linewidth of 6.6 meV, with carrier densities of $N_e=N_h=5 \times 10^{18}$ cm $^{-3}$ and a temperature of 300 K. The magnitude of the gain of the AKS model is very different compared with the six- and

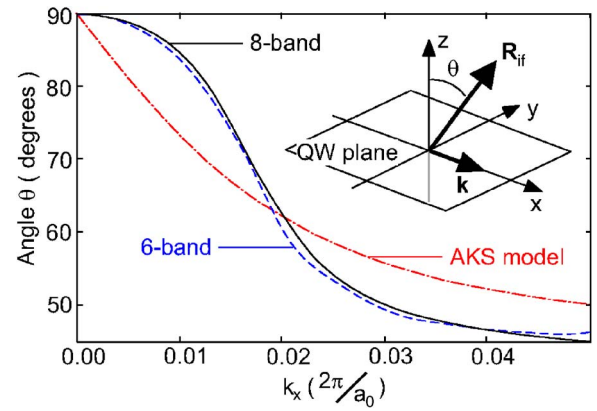


FIG. 10. (Color online) The deviation angle $\theta = \arccos(|\mathbf{R}_{if} \cdot \mathbf{u}_z|/|\mathbf{R}_{if}| |\mathbf{u}_z|)$ of the transition dipole $\mathbf{R}_{if} = \langle \Psi_{C1}(z, \mathbf{k}_{\parallel}) | \mathbf{p} | \Psi_{V1}(z, \mathbf{k}_{\parallel}) \rangle$ from the normal (z axis) of the QW plane as a function of $\mathbf{k}_{\parallel} = [k_x, 0]$. The solid, dashed, and dash-dotted lines correspond to the eight-band, six-band, and AKS models. Although θ is 90° at $\mathbf{k}_{\parallel} = \mathbf{0}$ and approaches 45° with increasing \mathbf{k}_{\parallel} , there is a large difference between the models for small but nonzero \mathbf{k} values.

eight-band $\mathbf{k} \cdot \mathbf{p}$ models due to larger transition amplitudes and slightly different quasi-Fermi energies. The quasi-Fermi energies were calculated from fixed carrier concentrations and since the DOS is smaller in the AKS model than in the eight- and six-band models, the quasi-Fermi energies are shifted deeper in the conduction/valence bands.

There is also a striking difference between the shape of the gains obtained with different models. The AKS gain model accounts only for the diagonal transitions and assumes that only valence bands with HH character take part in the recombination. However, the total gain is a sum of many transitions and also the nondiagonal transitions affect the exact gain profile. This is seen particularly in the gain of ϵ_{\parallel} polarized light. Note that, for larger transition linewidths, it becomes impossible to distinguish the different transitions from each other.

C. Geometrical relation between the transition dipole and the electron wave vector

An attractive feature in the analysis of Asada *et al.* is the use of the orthogonality between the transition dipole and the electron wave vector, in explaining the polarization of gain. Their procedure is based on the diagonalization of the linear eight-band bulk Hamiltonian. However, it is applicable only for bulk semiconductors. In the case of a QW the electron wave vector is, strictly speaking, defined only within the QW plane. The third component orthogonal to the QW plane is zero. However, Asada *et al.* assigned to this component an artificial value, calculated from the quantization energy.

In this work we restrict our calculations within exactly defined quantum mechanical quantities. Therefore, we have calculated the deviation θ of the transition dipole $\mathbf{R}_{if} = \langle \Psi_{C1}(z, \mathbf{k}_{\parallel}) | \mathbf{r} | \Psi_{V1}(z, \mathbf{k}_{\parallel}) \rangle$, from the normal of the QW plane, for the $C1 \rightarrow V1$ transition (see Fig. 10). The deviation angle was defined as $\theta = \arccos(|\mathbf{R}_{if} \cdot \hat{\mathbf{u}}_z|/|\mathbf{R}_{if}|)$. We have calculated angle θ as a function of $\mathbf{k}_{\parallel} = [k_x, 0]$, in order to study the rotation of \mathbf{R}_{if} in the different gain models. From Fig. 10

we observe that the transition dipole is in the QW plane ($\theta = 90^\circ$) for $\mathbf{k}_{\parallel} = \mathbf{0}$ and approaches $\theta = 45^\circ$ for large \mathbf{k}_{\parallel} values, in all gain models.

At the lower wave vector limit ($\mathbf{k}_{\parallel} \rightarrow 0$), $\theta = 90^\circ$, the valence band ground state is a pure HH state with mainly $|X\rangle$ and $|Y\rangle$ components. The transition dipole has therefore no z component. This agrees with the bulk case where the HH eigenstate of the Hamiltonian is decoupled when $z \parallel \mathbf{k}$. It is straightforward to see that with the generalized wave vector definition of the AKS model $\mathbf{k} \perp \mathbf{R}_{if}$ for $\mathbf{k}_{\parallel} = 0$.

The upper asymptotic limit $\mathbf{k}_{\parallel} \rightarrow 0.05 \times k_{Bz}$ corresponds to a complex transition dipole of type $\mathbf{R}_{if} \sim |z\rangle + i|y\rangle$. This corresponds in the AKS model to a 90° rotation of the transition dipole around the y axis. For large \mathbf{k}_{\parallel} values the effect of the \mathbf{k}_z operator on the eight-band Hamiltonian decreases and the results are dominated by the \mathbf{k}_{\parallel} -dependent terms. Therefore, the results of the eight-band and AKS models agree at the upper asymptotic limit as well.

The results based on the AKS model differ significantly from the multiband models although the asymptotic limits are the same. This applies mainly to the gain of ϵ_{\perp} polarized light. In the six- and eight-band $\mathbf{k} \cdot \mathbf{p}$ models the main peak of the gain is due to the $C1 \rightarrow V2$ ($V2 = LH1$) transition at $\mathbf{k}_{\parallel} \approx \mathbf{0}$, since the transition dipole of the $C1 \rightarrow V1$ transition is practically perpendicular to the ϵ_{\perp} electric field for all occupied states. However, in the AKS model the peak gain of the ϵ_{\perp} polarized light is due to the $C1 \rightarrow V1$ ($V1 = HH1$) at $\mathbf{k}_{\parallel} \neq \mathbf{0}$, because there are no other allowed radiative transitions close to the band edge. Figure 10 shows also that the rotation of the transition dipole in the six- and eight-band $\mathbf{k} \cdot \mathbf{p}$ models is very similar. We conclude that the perturbative treatment of the conduction-valence band coupling, which is included in the six-band model (see Appendix), is fairly accurate.

V. CONCLUSIONS

In conclusion we have found that while the rotating dipole model of Asada *et al.* (AKS) works well for the electronic structure of bulk semiconductors, there are several reasons why it fails in quantitative predicting the polarization of gain of QW lasers: (1) Although, the idea of eigenstates that rotate with the direction of \mathbf{k} is qualitatively correct also for QWs, the exact dependence on \mathbf{k}_{\parallel} is not very accurate. (2) The AKS model can only account for the diagonal transitions $Ci \rightarrow Vi$. Furthermore, the AKS model (3) excludes the LH bands and (4) simplifies the interband coupling. Finally, (5) the transition amplitudes are overestimated. We found that points (2)–(4) together severely simplify the transition spectrum of the studied polarizations and redshift the peak gain of the ϵ_{\perp} (TM) polarization. Note also that the origin of the TM mode in our eight-band model is in the nondiagonal transitions whereas it, in the AKS model, originates from the $C1 \rightarrow V1$ transition at $\mathbf{k}_{\parallel} \neq 0$. The LH band must be included as well as the valence band mixing, in order to obtain a correct polarization-dependent gain profile. We also found it very difficult to improve the AKS model without losing its simple analytical form.

We have found that the differences, in the calculated polarization of the gain, between the six- and eight-band $\mathbf{k} \cdot \mathbf{p}$

models are small and come from the contributions of higher excited bands. The differences between the six- and eight-band models increase with increasing energy and electron wave vector \mathbf{k} . This, however, does not affect the polarization of the gain very much, because it depends mainly on the band structure close to the band edge.

The present calculations of gain polarization do not include carrier-carrier interactions. On the microscopic scale, the polarization of photon emission is governed by the directional properties of electronic orbitals of the pertinent electric dipole amplitudes. The correlation (carrier-carrier) effects influence the anisotropy of the transition amplitude if the two-particle correlation is strong enough (exciton regime) to change the pertinent single-particle orbitals. However, all our calculations correspond to carrier densities at which the exciton resonance disappears.²⁷ The correlation affects therefore the transition dipole mainly via a screened carrier-carrier interaction. As shown by Hader *et al.*, the most prominent influence of the Coulomb interaction, in this limit, is a blue-shift of the gain maximum with increasing carrier density.¹⁰ However, the screened Coulomb effect is nearly isotropic and we expect that its influence on the gain polarization is less important. Ellmers *et al.* have made a detailed comparison of experimental and theoretical gain spectra for an InGaN single QW laser diode.¹² In their work they obtained a complete quantitative agreement between theory and experiments only by including many-body Coulomb effects as well as using a microscopic treatment of carrier scattering and polarization dephasing. However, the complete agreement between theory and experiments was obtained using the four-band Luttinger-Kohn Hamiltonian which is known to be rather inaccurate for the description of the electronic structure. Nevertheless, the influence of the Coulomb effect on the polarization of gain is an important topic of further studies. On the basis of our work we suggest that in calculations of the gain polarization, based on semiconductor Bloch equations, the quality of the $\mathbf{k} \cdot \mathbf{p}$ parameters should be verified by pseudopotential calculations. Furthermore, we emphasize the role of the nondiagonal transitions, especially in the calculation of the TM mode.

APPENDIX: EIGHT-BAND $\mathbf{k} \cdot \mathbf{p}$ MODEL OF ZINC BLENDE CRYSTALS

The eight-band $\mathbf{k} \cdot \mathbf{p}$ model (see, e.g., Ref. 28 and references therein) has been developed for electronic structure calculations of direct-band semiconductors in the vicinity of Γ point, i.e., $\mathbf{k} = 0$. The bulk and quantum confined electron states are described as linear combinations of atomic Bloch functions. The Bloch functions are in turn expanded in terms of the perturbatively projected Γ -point atomic Bloch functions $|u_{\nu}(\mathbf{r})\rangle$ by

$$|u_{\alpha}(\mathbf{k}, \mathbf{r})\rangle = \sum_{\nu=1}^8 C_{\nu}^{\alpha}(\mathbf{k}) |u_{\nu}(\mathbf{r})\rangle, \quad (\text{A1})$$

where $C_{\nu}^{\alpha}(\mathbf{k})$ are the mixing coefficients. The *projected* Bloch functions are given by

$$|u_\nu(\mathbf{r})\rangle = |u_\nu^0(\mathbf{r})\rangle + \sum_{m \notin A} \frac{\hbar}{m_0} |u_m^0(\mathbf{r})\rangle \frac{\langle u_m^0(\mathbf{r}) | \mathbf{k} \cdot \mathbf{p} | u_\nu^0(\mathbf{r}) \rangle}{E_\nu^0 - E_m^0}, \quad (\text{A2})$$

where $|u_i^0(\mathbf{r})\rangle$ are the Γ -point atomic Bloch functions and E_i^0 are their energies evaluated at $\mathbf{k}=0$.

The eight strongly coupled Bloch functions [states A in Eq. (A2)] are treated by direct diagonalization and assumed independent on the heterostructure material.²⁹ The remaining states $m \notin A$ are accounted for by perturbation theory.^{30,31} In this work we have used the following eight Bloch functions of group A :

$$\begin{aligned} |u_1\rangle &= i|S\uparrow\rangle, & \Gamma_6, \\ |u_2\rangle &= i|S\downarrow\rangle, & \Gamma_6, \\ |u_3\rangle &= \frac{1}{\sqrt{2}}(|X\uparrow\rangle + i|Y\uparrow\rangle), & \Gamma_8, \\ |u_4\rangle &= \frac{i}{\sqrt{6}}(|X\downarrow\rangle + i|Y\downarrow\rangle) - i\sqrt{\frac{2}{3}}|Z\uparrow\rangle, & \Gamma_8, \\ |u_5\rangle &= \frac{1}{\sqrt{6}}(|X\uparrow\rangle - i|Y\uparrow\rangle) + \sqrt{\frac{2}{3}}|Z\downarrow\rangle, & \Gamma_8, \\ |u_6\rangle &= \frac{i}{\sqrt{2}}(|X\downarrow\rangle - i|Y\downarrow\rangle), & \Gamma_8, \\ |u_7\rangle &= \frac{1}{\sqrt{3}}(|X\downarrow\rangle + i|Y\downarrow\rangle + |Z\uparrow\rangle), & \Gamma_7, \\ |u_8\rangle &= -\frac{i}{\sqrt{3}}(|X\uparrow\rangle - i|Y\uparrow\rangle - |Z\downarrow\rangle), & \Gamma_7, \end{aligned} \quad (\text{A3})$$

which span the eight-dimensional subspace of the irreducible representations Γ_6 , Γ_8 , and Γ_7 of the T_d symmetry group, associated with the zinc blende crystal. In this basis the eight-band $\mathbf{k} \cdot \mathbf{p}$ Hamiltonian of bulk semiconductors is given by

$$H = \begin{pmatrix} A & 0 & -i\sqrt{3}P_+ & -\sqrt{2}P_z & -iP_- & 0 & -iP_z & -\sqrt{2}P_- \\ A & 0 & P_+ & -i\sqrt{2}P_z & \sqrt{3}P_- & -i\sqrt{2}P_+ & P_z & \\ & -Q-P & iS & \mathcal{R} & 0 & -S/\sqrt{2} & -i\sqrt{2}\mathcal{R} & \\ & & Q-P & 0 & \mathcal{R} & i\sqrt{2}Q & -\sqrt{\frac{3}{2}}S & \\ & & & Q-P & -iS & -\sqrt{\frac{3}{2}}S^* & i\sqrt{2}Q & \\ & & & & -Q-P & -i\sqrt{2}\mathcal{R}^* & -S^*/\sqrt{2} & \\ & & & & & Z & 0 & \\ & & & & & & & Z \end{pmatrix}, \quad (\text{A4})$$

where we have defined the following parameters:

$$A = E_c + \gamma_c \frac{\hbar^2 k^2}{2m_0} + a_c(\varepsilon_{xx} + \varepsilon_{yy} + \varepsilon_{zz}), \quad (\text{A5a})$$

$$P = -E_v + \gamma_1 \frac{\hbar^2 k^2}{2m_0} - a_v(\varepsilon_{xx} + \varepsilon_{yy} + \varepsilon_{zz}), \quad (\text{A5b})$$

$$Q = \gamma_2 \frac{\hbar^2}{2m_0} (k_x^2 + k_y^2 - 2k_z^2) - \frac{b_v}{2} (\varepsilon_{xx} + \varepsilon_{yy} - 2\varepsilon_{zz}), \quad (\text{A5c})$$

$$Z = E_v - \Delta - \gamma_1 \frac{\hbar^2 k^2}{2m_0} + a_v(\varepsilon_{xx} + \varepsilon_{yy} + \varepsilon_{zz}), \quad (\text{A5d})$$

$$P_z = \frac{1}{\sqrt{3}} \left(i\hbar \sqrt{\frac{E_p}{2m_0}} k_z + Bk_x k_y \right), \quad (\text{A5e})$$

$$P_\pm = \frac{1}{\sqrt{6}} \left[i\hbar \sqrt{\frac{E_p}{2m_0}} (k_x \pm ik_y) + Bk_z (k_y \pm ik_x) \right], \quad (\text{A5f})$$

$$S = \sqrt{3} \gamma_3 \frac{\hbar^2}{m_0} k_z (k_x - ik_y) + d_v (i\varepsilon_{yz} - \varepsilon_{xz}), \quad (\text{A5g})$$

$$\begin{aligned} \mathcal{R} = & -\sqrt{3} \frac{\hbar^2}{2m_0} [\gamma_2 (k_x^2 - k_y^2) - 2i\gamma_3 k_x k_y] - \frac{\sqrt{3}b_v}{2} (\varepsilon_{xx} - \varepsilon_{yy}) \\ & - id_v \varepsilon_{xy}. \end{aligned} \quad (\text{A5h})$$

In Eqs (A4) and (A5), E_c (E_v) is the position of the conduction (valence) band edge, Δ is the spin-orbit splitting energy, and B is Kane's band parameter related to inversion asymmetry in a zinc blende crystal. Furthermore, ε_{ij} are the components of the strain tensor, and a_c , a_v , b_v , and d_v are the related deformation potentials. The modified Luttinger parameters are related to the original Luttinger parameters (denoted as γ_i^L) by

$$\gamma_1 = \gamma_1^L - \frac{E_p}{3E_g}, \quad (\text{A6a})$$

$$\gamma_2 = \gamma_2^L - \frac{E_p}{6E_g}, \quad (\text{A6b})$$

$$\gamma_3 = \gamma_3^L - \frac{E_p}{6E_g}. \quad (\text{A6c})$$

The six-band $\mathbf{k} \cdot \mathbf{p}$ model is obtained from the eight-band model by substituting $P_0=0$ and $B=0$. This decouples the six valence bands from the conduction band. Moreover, in the eight-band model the C band belongs to group A , whereas it is treated as a distant band in the six-band model. The γ parameters of the $\mathbf{k} \cdot \mathbf{p}$ Hamiltonian account for the effect of distant band and, as a result, the γ parameters are different in the six- and eight-band models.

1. $\mathbf{k} \cdot \mathbf{p}$ model for quantum wells

The eight-band $\mathbf{k} \cdot \mathbf{p}$ model can be used to calculate the electronic structure of low-dimensional semiconductor structures using the envelope wave function approximation.³² However, the parameters of the model are always fitted to experimental or theoretical band gaps and effective masses, at the Γ point of the pertinent bulk semiconductors. In the case of a QW (grown along the z axis) we first write all matrix elements of the Hamiltonian symmetrically and replace the z component of \mathbf{k} by the operator $k_z = k_{\perp} \rightarrow -i\partial/\partial z$. Then we denote the in-plane wave vector by $\mathbf{k}_{\parallel} = [k_x, k_y]$. Finally, all derivatives were replaced by symmetrized finite differences

$$\frac{\partial}{\partial z} g_j \Psi_j \rightarrow \frac{1}{4\Delta z} \{ [g_{j+1} + g_j] \Psi_{j+1} - [g_j + g_{j-1}] \Psi_{j-1} \}, \quad (\text{A7a})$$

$$\begin{aligned} \frac{\partial}{\partial z} g_j \frac{\partial}{\partial z} \Psi_j \rightarrow & \frac{1}{2\Delta z^2} \{ [g_{j+1} + g_j] \Psi_{j+1} - [g_{j+1} + 2g_j + g_{j-1}] \Psi_j \\ & + [g_j + g_{j-1}] \Psi_{j-1} \}, \end{aligned} \quad (\text{A7b})$$

where g is any position dependent material parameter, Ψ is the differentiated wave function, Δz is the spacing of two neighboring grid points, and the subindices represent the z coordinate. This ensured that the differentiated Hamiltonian was Hermitian. In the case of an (111) QW, a coordinate transformation of \mathbf{k} and \mathbf{r} had to be done before the differentiation.³³

The wave functions in a QW geometry are given by

$$\Psi_\alpha(\mathbf{r}, \mathbf{k}_{\parallel\alpha}) = N e^{i\mathbf{k}_{\parallel\alpha} \cdot \mathbf{r}_{\parallel\alpha}} \sum_{\nu=1}^8 \phi_\nu^\alpha(z, \mathbf{k}_{\parallel\alpha}) |u_\nu(\mathbf{r})\rangle, \quad (\text{A8})$$

where we have replaced the mixing coefficients by the envelope wave functions $\phi_\nu^\alpha(z, \mathbf{k}_{\parallel\alpha})$. The envelope wave functions were obtained as the eigenstates of the envelope Hamiltonian (depends now on z) given in Eq. (A4). For a thorough description of the eight-band $\mathbf{k} \cdot \mathbf{p}$ model, see Refs. 13, 19, 20, 22, and 28.

¹M. Asada, A. Kameyama, and Y. Suematsu, IEEE J. Quantum Electron. **20**, 745 (1984).

²M. Yamada, S. Ogita, M. Yamagishi, K. Tabata, N. Nakaya, M. Asada, and Y. Suematsu, Appl. Phys. Lett. **45**, 324 (1984).

³P. J. Mares and S. L. Chuang, J. Appl. Phys. **74**, 1388 (1993).

⁴T. Fleischmann, M. Moran, M. Hopkinson, H. Meidia, G. J. Rees, A. G. Cullis, J. L. Sánchez-Rojas, and I. Izpura, J. Appl. Phys. **89**, 4689 (2001).

⁵P. A. Chen, C. Y. Chang, and C. Juang, J. Appl. Phys. **76**, 85 (1994).

⁶D. Ahn and S.-L. Chuang, IEEE J. Quantum Electron. **24**, 2400 (1988).

⁷M. S. Wartak and P. Weetman, J. Appl. Phys. **95**, 3834 (2004).

⁸D. Ahn, IEEE J. Quantum Electron. **32**, 960 (1996).

⁹D. Gershoni, C. H. Henry, and G. A. Baraff, IEEE J. Quantum Electron. **29**, 2433 (1993).

¹⁰J. Hader, J. V. Moloney, S. W. Koch, and W. W. Chow, IEEE J. Sel. Top. Quantum Electron. **9**, 688 (2003).

¹¹A. Girndt, F. Jahnke, A. Knorr, S. W. Koch, and W. W. Chow, Phys. Status Solidi B **202**, 725 (1997).

¹²C. Ellmers *et al.*, Phys. Status Solidi B **206**, 407 (1998).

¹³E. Kane, J. Phys. Chem. Solids **1**, 249 (1957).

¹⁴M. Yamada, S. Ogita, M. Yamagishi, and K. Tabata, IEEE J. Quantum Electron. **21**, 640 (1985).

¹⁵D. L. Smith and C. Mailhot, Rev. Mod. Phys. **62**, 173 (1990).

¹⁶B. A. Foreman, Phys. Rev. B **56**, R12748 (1997).

¹⁷M. Yamanishi and I. Suemune, Jpn. J. Appl. Phys., Part 1 **23**, 35 (1984).

¹⁸R. H. Yan, S. W. Corzine, L. A. Coldren, and I. Suemune, IEEE J. Quantum Electron. **26**, 213 (1990).

¹⁹G. L. Bir and G. E. Pikus, *Symmetry and Strain-Induced Effects in Semiconductors* (Wiley, New York, 1974).

²⁰C. Mailhot and D. L. Smith, Phys. Rev. B **33**, 8345 (1986).

²¹J. W. Thomas, *Numerical Partial Differential Equations* (Springer, New York, 1995).

²²C. Mailhot and D. L. Smith, Phys. Rev. B **33**, 8360 (1986).

²³C. Mailhot and D. L. Smith, Phys. Rev. B **35**, 1242 (1987).

²⁴S. v. Alftan, F. Boxberg, K. Kaski, A. Kuronen, R. Tereshonkov, J. Tulkki, and H. Sakaki, Phys. Rev. B **72**, 045329 (2005).

²⁵N. W. Ashcroft and N. D. Mermin, *Solid State Physics* (Sanders College, Hong Kong, 1987), p. 143.

²⁶P. Enders, A. Barwolff, M. Woerner, and D. Suisky, Phys. Rev. B **51**, 16695 (1995).

²⁷J. P. Loehr and J. Singh, Phys. Rev. B **42**, 7154 (1990).

²⁸T. B. Bahder, Phys. Rev. B **41**, 11992 (1990).

²⁹M. G. Burt, J. Phys.: Condens. Matter **4**, 6651 (1992).

³⁰P. Löwdin, J. Chem. Phys. **19**, 1396 (1951).

³¹J. P. Loehr, Phys. Rev. B **52**, 2374 (1995).

³²G. Bastard, Phys. Rev. B **24**, 5693 (1981).

³³G. A. Baraff and D. Gershoni, Phys. Rev. B **43**, 4011 (1991).